




EMERGING MECHANISMS FOR ENHANCED PLASTICITY IN MAGNESIUM

The Effect of Grain Size on the Bend Forming Limits in AZ31 Mg Alloy

S.H. MOHAMADI AZGHANDI ^{1,2}, M. WEISS,¹ and M.R. BARNETT¹

1.—Institute for Frontier Materials, Deakin University, Geelong, VIC 3216, Australia.
2.—e-mail: h.mohamadiazghandi@deakin.edu.au

The present study examines the bending behavior of coarse and fine-grained AZ31 magnesium alloy. The corresponding deformation mechanisms are ascertained via tensile, compression, and bending tests in combination with digital image correlation and electron backscatter diffraction. It is shown that grain refinement from 60 μm to 3 μm significantly improves tensile ductility, while forming limits in compression and bending show no obvious effect of grain size. Analysis of the microstructure revealed a high density of twin bands in the compression zones of the bent samples. Interestingly, the fine-grained material experienced failure in the compression zone. The fracture strain in bending appears limited by the material ductility in both tension and compression. The outcome of this study is that in magnesium alloys grain refinement may not always be an effective method for the improvement of ductility, particularly when bending of the type considered here is dominant.

INTRODUCTION

Magnesium and its alloys are the lightest metallic structural materials with high specific strength and bending stiffness.¹ However, magnesium has a low number of active slip systems due to its hexagonal close-packed (HCP) crystal structure, resulting in low room temperature formability.² Bending is one of the major deformation modes in sheet forming.^{3,4} The bend limit of magnesium alloys, which is the ratio of the minimum bent radius to the sheet thickness, is often reported to fall in the range 3–5.^{5,6} It has also been found that the bend limit of magnesium alloys depends on the crystallographic texture,^{7–12} strain rate^{10,13} and temperature.^{14–16} Recent work^{17,18} showed that the cumulative bendability of AZ31 can be improved by annealing. However, the low bendability of magnesium alloys can still limit its application. Datsko's work⁵ suggested a relationship between the reduction in area in a tensile test and the bendability of metals such that alloys with higher reduction in area possess higher bendability (a lower bend limit). Grain refinement generally improves the tensile ductility (e.g., reduction in area) and strength simultaneously in many magnesium alloys.^{6,19–30} However, its influence on bendability is still unclear.

While tensile ductility has been widely examined, bendability has received much less attention. In particular, the influence of grain size on the bending limit appears not to have been explicitly investigated. The present study seeks to determine the role of grain size on the bendability of AZ31 Mg alloy.

MATERIALS AND METHODS

Materials

As-received AZ31 alloy³¹ was cut into 10-mm-thick plate and hot-rolled at 300°C in 4 clock-rolling passes with a reduction in thickness of 33% in each pass, using a 2000 kN rolling mill. The plate was reheated for 5 min between each pass. The 2-mm sheet produced was annealed at 230°C for 1 h and 500°C for 24 h in an argon atmosphere controlled muffle furnace. Final sheets with average grain sizes of 3 μm and 60 μm and a typical basal texture were produced (Fig. 1). The normalized grain size distributions can be seen in Fig. 1e and f. Both materials contain Al-Mn second-phase particles,³¹ with their volume fractions and sizes being approximately the same between the coarse- and the fine-grained alloy.

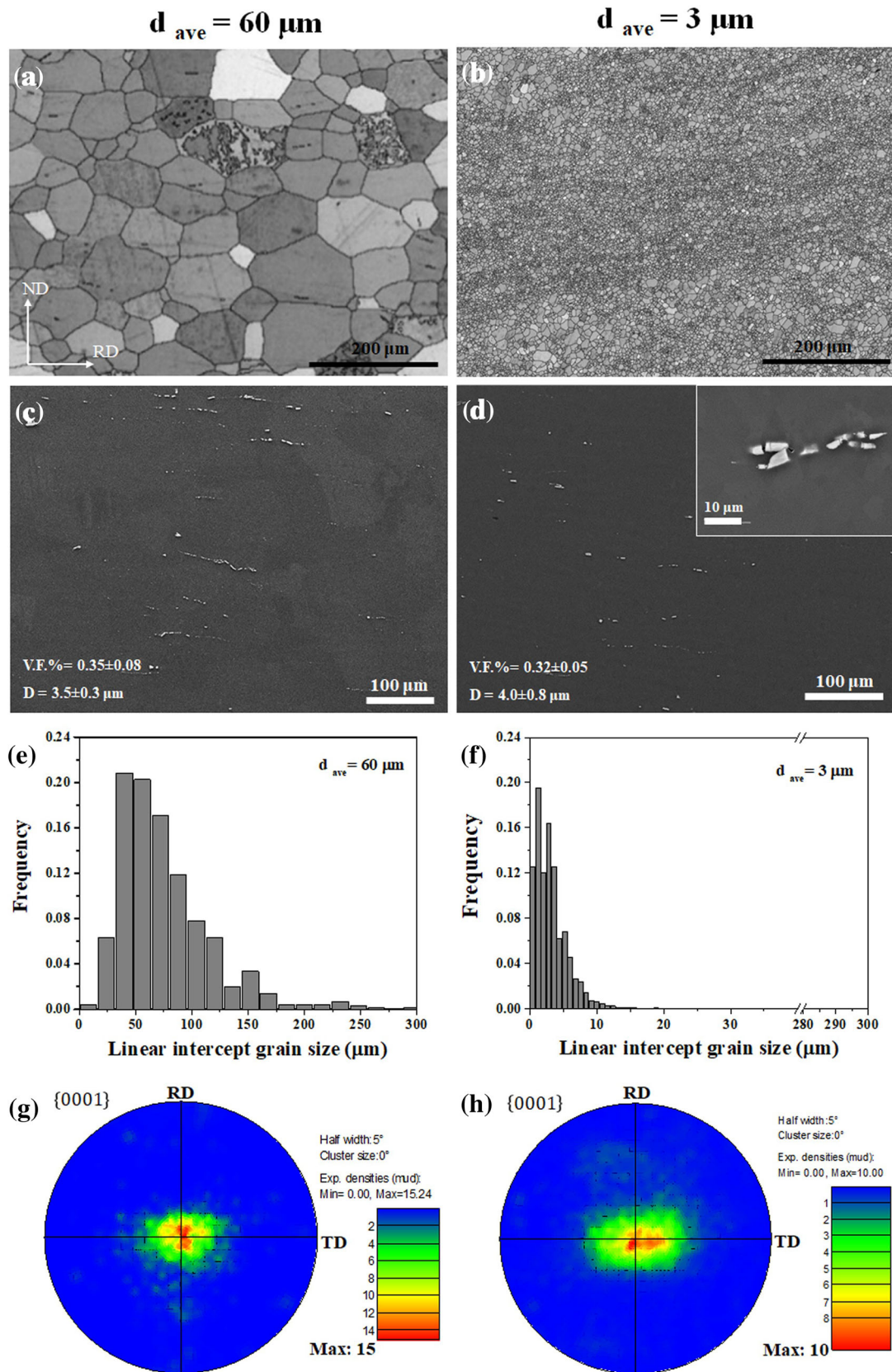


Fig. 1. Initial microstructures (a–d) showing grains (a, b) and second-phase particles (c, d), grain size distribution (e, f), and texture (g, h) of the materials with average grain sizes of 60 μm and 3 μm .

Mechanical Testing

Tensile specimens were prepared along the transversal direction (TD) with a gauge length of 25 mm according to ASTM-B557M.³ Cube shaped compression samples of 4 mm × 2 mm × 2 mm were machined from the sheet materials using electrical-discharge machining.³² Tensile and compression tests were carried out along the TD using 30-kN and 5-kN Instron machines, respectively, at a strain rate of $1 \times 10^{-3} \text{ s}^{-1}$ and using a video extensometer to measure strain. A three-point bending test was conducted on specimens of $100 \times 20 \times 2 \text{ mm}$ along the TD (bending line parallel to TD) in an Erichsen sheet metal tester with a specially designed fixture and a sharp punch radius of 0.2 mm (Fig. 2a). The GOM-ARAMIS system was employed for the in situ measurement of principal bending strain.

The GOM-ARAMIS system was employed to measure the principal bending strain on the outer surface of the bent specimen (Fig. 2b). To measure the outer bend radius a cylinder was fitted to the bent area. The radius at the maximum punch force (R_o) was employed to calculate the bend limit⁵ as follows:

$$\text{Bend limit} = \frac{R_i}{t} \quad (1)$$

where t is the thickness of the sheet and R_i is bending radius of the inner surface at maximum force (obtained by $R_i = R_o - t$).

Microstructure Analysis

Samples were ground with 1200 grit SiC paper followed by mechanical polishing with diamond paste from 9 to 6 μm to 3 μm with a final polish of colloidal silica slurry. After this, the samples were immersed in acetic picral solution (100 mL ethanol, 10 mL H_2O , 6 g picric acid, 5 mL acetic acid) for 5–15 s. The as-polished samples were evaluated by electron backscatter diffraction (EBSD) to determine the average grain size, the crystallographic orientation and the twinning systems. Oxford HKL channel 5 software was used to analyze the EBSD maps. The average grain size was measured on 8000 grains, based on the linear intercept method² with a critical misorientation angle of 15° . The crystallographic textures were determined from electron-backscattered diffraction maps of ~ 8000 grains. To evaluate the second-phase particles, approximately 2.5 mm^2 area (about 1000 particles) of each sample was examined. In this examination, only particles that were larger than 1 μm were taken into account.

RESULTS

Mechanical Response

Figure 3 and Table I show the mechanical properties of the present samples in tension, compression and bending. Both materials show similar plastic anisotropy (r_{value}) and strain hardening (n_{value}) of 3 ± 0.4 and 0.2 ± 0.01 , respectively. The tensile and compressive yield and peak strengths

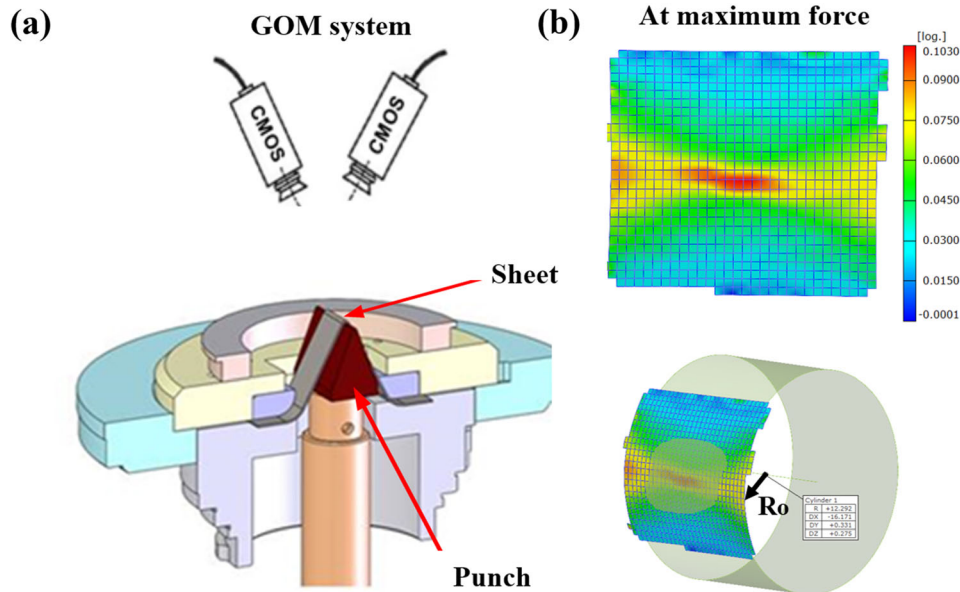


Fig. 2. (a) Schematic of the three-point bending test implemented in an Erichsen sheet metal tester in combination with a GOM-ARAMIS system, and (b) an example of the principal bending strain map of the outer bend surface at the maximum bending force and the fitted cylinder shape to measure the outer radius (R_o).

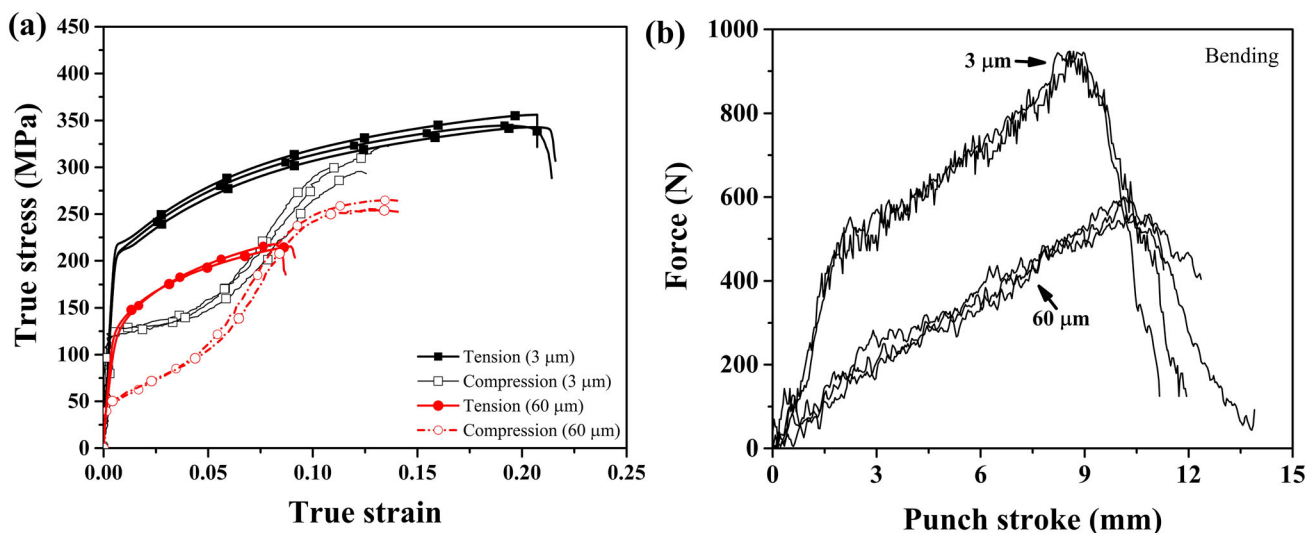


Fig. 3. (a) True stress–strain curves in tension and compression and (b) bending force–displacement curves of the materials with grain sizes of 60 μm and 3 μm .

increase with grain refinement. This leads to higher punch forces when bending the fine-grained alloy compared to the coarse-grained material (Fig. 3b). The yield asymmetry ($\sigma_{Y,T}/\sigma_{Y,C}$) reduces from 2.8 to 1.7 with decreasing grain size from 60 μm to 3 μm . The tensile ductility ($\varepsilon_{u,T}$, $\varepsilon_{f,T}$, R_A) significantly improves with grain refinement. In contrast to this the ductility in compression ($\varepsilon_{f,C}$) and the fracture limit strain in bending ($\varepsilon_{\text{max},B}$), i.e., the bendability (R_i/t) do not change with grain refinement.

Strain Analysis

The strain distribution on the outer surface of the coarse- and fine-grained materials during bending can be observed in Fig. 4a and b, respectively. The corresponding force values are highlighted by red dots in Fig. 4c. Strain localization occurs in the middle of the sheet. The evolution of strain shows an almost linear trend followed by an abrupt increase in strain when F_{max} is reached (Fig. 4c). This abrupt increase is likely due to flow localization followed by crack initiation just after the maximum bend force is reached. The strain maps show that this occurs in the mid-section of the strip, where the strain most closely approaches plane strain.

The bending strain at maximum force is 0.115 and 0.105 in the coarse- and fine-grained materials, respectively. Figure 5 shows the appearance of the speckle pattern just after reaching the maximum force. These images reveal irregularities of the surface that mark the onset of surface failure. The strain at maximum bending force is taken as the maximum bending strain. The bending curve of fine-grained alloy shows two stages, corresponding to elastic and plastic regions. However, the coarse-grained material yields at low loads and thus a clear

elastic region is not easily distinguished. In addition, the tensile data show that the coarse-grained alloy displays smooth yielding and this is accentuated in bending.

Microstructure

In the coarse-grained material, fracture initiates only on the outer surface (tension zone), while the fine-grained material experiences failure in both the outer and inner surfaces (Fig. 6). The mid cross section images show the propagated cracks beyond the point of maximum bend force (the corresponding force–time relationship can be seen in Fig. 5c).

Figure 7 shows the deformed microstructures of samples bent close to the maximum force. In the tension zone of the coarse-grained material, twin bands are seen near the outer surface and $\{10\bar{1}1\}\{10\bar{1}2\}$ double twin and $\{10\bar{1}1\}$ compression twin boundaries can be detected (Fig. 7a1). In the tension zone of the fine-grained material, the highly distorted microstructure includes fine twins close to the outer surface (white arrows Fig. 7b1). Traces of $\{10\bar{1}1\}$ compression twins and $\{10\bar{1}1\}\{10\bar{1}2\}$ double twins were also observed. The local strain is $\varepsilon = 0.09$ in the tension zone of both materials. A higher number density of twins and coarser twins were observed in the coarse-grained material, compared to the fine-grained counterpart.

In the compression zone, $\{10\bar{1}2\}$ tension twin boundaries were found (Fig. 7a2 and b2) in combination with a second twin boundary type (highlighted in green). This type showed rotation axes of 0110 and an angle of 58° which correspond to boundaries formed by twin–twin interaction between different $\{10\bar{1}2\}$ twin variants.³³ Very close to the inner surface, twin bands were revealed

Table I. Mechanical properties of the materials with grain sizes of 60 μm and 3 μm ($\sigma_{Y,T}$, $\sigma_{Y,C}$ are tensile and compressive yield strength, $\varepsilon_{u,T}$, $\varepsilon_{f,T}$, R_A , $\varepsilon_{f,C}$, $\varepsilon_{\text{max},B}$ are tensile uniform strain, tensile total strain, reduction in area, compressive total strain, and bending strain at maximum bending force F_{max})

$d(\mu\text{m})$	Tension			Compression			Bending		
	$\sigma_{Y,T}$ (MPa)	$\varepsilon_{u,T}$	$\varepsilon_{f,T}$	R_A (%)	$\sigma_{Y,C}$ (MPa)	$\varepsilon_{f,C}$	F_{max} (N)	$\varepsilon_{\text{max},B}$	Bend limit (R_i/t)
60	123 \pm 5	0.09 \pm 0.008	0.094 \pm 0.01	16.5 \pm 0.7	44 \pm 1	0.14 \pm 0.005	553 \pm 6	0.115 \pm 0.01	4.23 \pm 0.2
3	217 \pm 6	0.15 \pm 0.001	0.23 \pm 0.01	34.5 \pm 3.7	128 \pm 3	0.125 \pm 0.02	913 \pm 20	0.105 \pm 0.01	3.96 \pm 0.2

with traces of $\{10\bar{1}1\}\{10\bar{1}2\}$ double twin boundaries. As would be expected, the deformed textures in the tension and compression zones are different. In the tension zones, both materials retained the basal texture ($\{0001\}$ basal plane parallel to sheet plane); similar to an undeformed texture. In the compression zone, both materials developed a prism texture ($\{10\bar{1}0\}$ plane parallel to the sheet plane). This was related to a high activity of $\{10\bar{1}2\}$ tension twinning in the compression zone, which led to a rotation of the basal plane by approximately 86° (Fig. S1 in supplementary material).

Figure 8 shows the microstructure of the bent samples after crack formation. Importantly, very little void formation was observed outside of the shear localizations. In the tension zone (Fig. 8a1 and b1) cracks initiated along twin bands which were composed of double twin and compression twin boundaries. The calculated Schmid factor of the basal slip in the double twinned regions was markedly higher (~ 0.46) than in the untwinned neighboring matrix (Fig. S2 and Table S1 in supplementary material). In some cases, high Schmid factors were also found in the compression twins. The orientation of the double twinned regions was more favorable for basal slip, which can assist damage initiation through step formation. The twin bands are distinguished in two orientations; parallel and approximately perpendicular to the initiated cracks, which leads to a zigzag pattern of crack propagation.

In the compression zones (Fig. 8a2 and b2), twin bands are also evident and there is evidence of $\{10\bar{1}1\}\{10\bar{1}2\}$ double twinning. Cracking in the inner bend surface was only observed in the fine-grained material. Figure 8b2 shows that here the crack initiated and propagated along the twin bands, which includes $\{10\bar{1}1\}\{10\bar{1}2\}$ double twins. The bands of twins were formed at a prior deformation stage. It may be that the high loads in the fine-grained material lead to the initiation of localization, at least in the compression zone, at lower strains.

DISCUSSION

Grain refinement influences the bending behavior of the AZ31 magnesium alloy such that the bending strength increases with reducing grain size. This can be rationalized by the increase of both tensile and compressive strength with grain refinement.

However, the maximum bending strain and bendability (R_i/t) do not show a pronounced change with the grain size. There are two key points to be made that help to explain this observation. The first is that grain refinement is seen to lead to a higher ductility in tension tests and not in compression tests (Fig. 3a). Because bending involves both compression and tension, it is to be expected that it reflects at least a

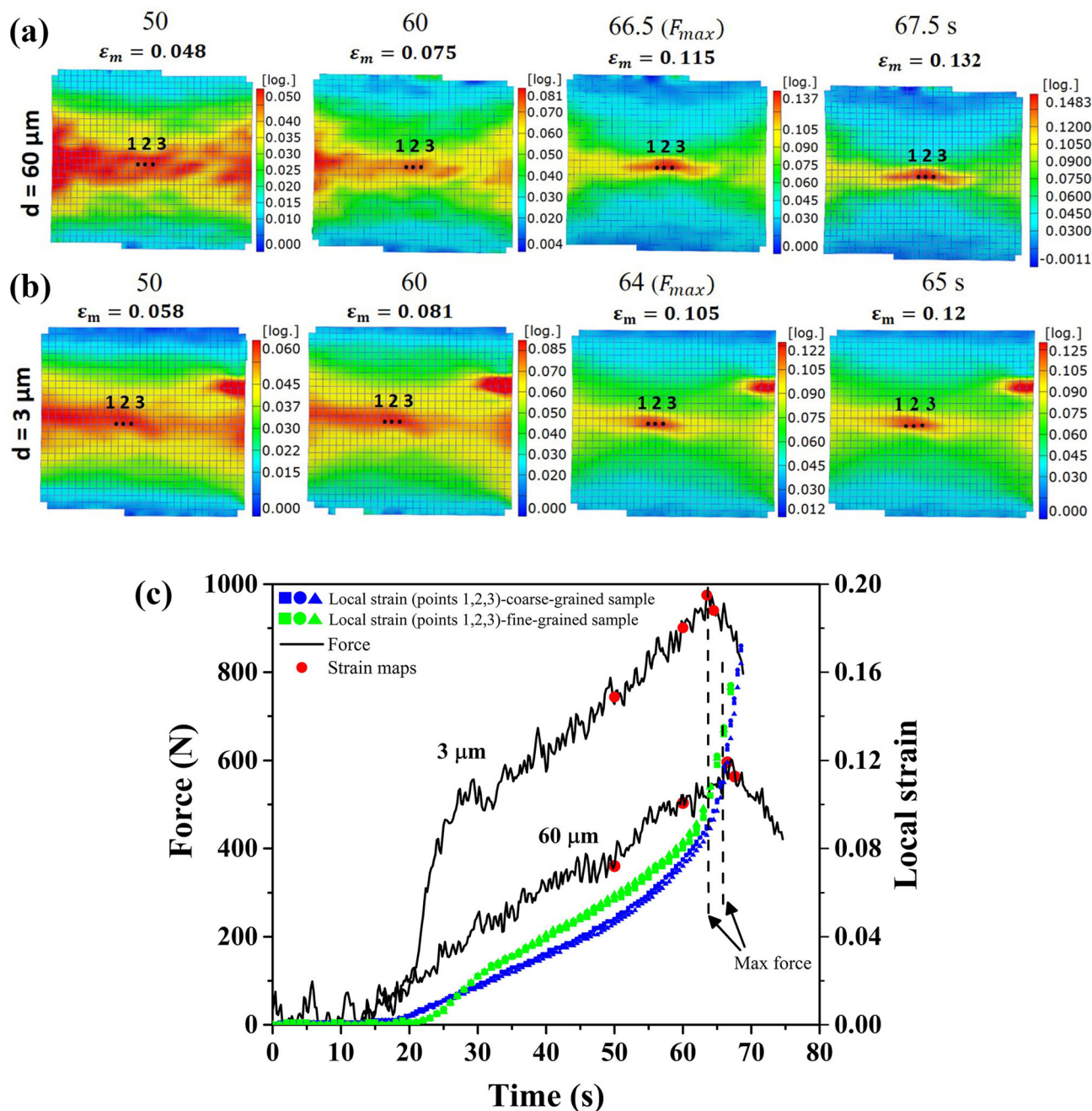


Fig. 4. DIC results of the coarse- and fine-grained materials during the bending test; (a, b) strain distribution of the outer surface of the bent sheet (the corresponding time and ϵ_m , the average strain of points 1, 2, 3 are shown) and (c) the corresponding force and local strain versus time (local strain is the average strain of points 1, 2, and 3).

combination of the grain size phenomena seen in the tension and compression tests. However, in the present study the failure on the outer tension side of the bend appears to occur at more or less the same strain for the two grain sizes. There is some uncertainty associated with this observation,

because the strain is localizing rapidly at the peak load. For this reason it is difficult to be completely sure of the local strain that precisely correlates with material failure. However, there is no evidence of a significant difference in failure strain.

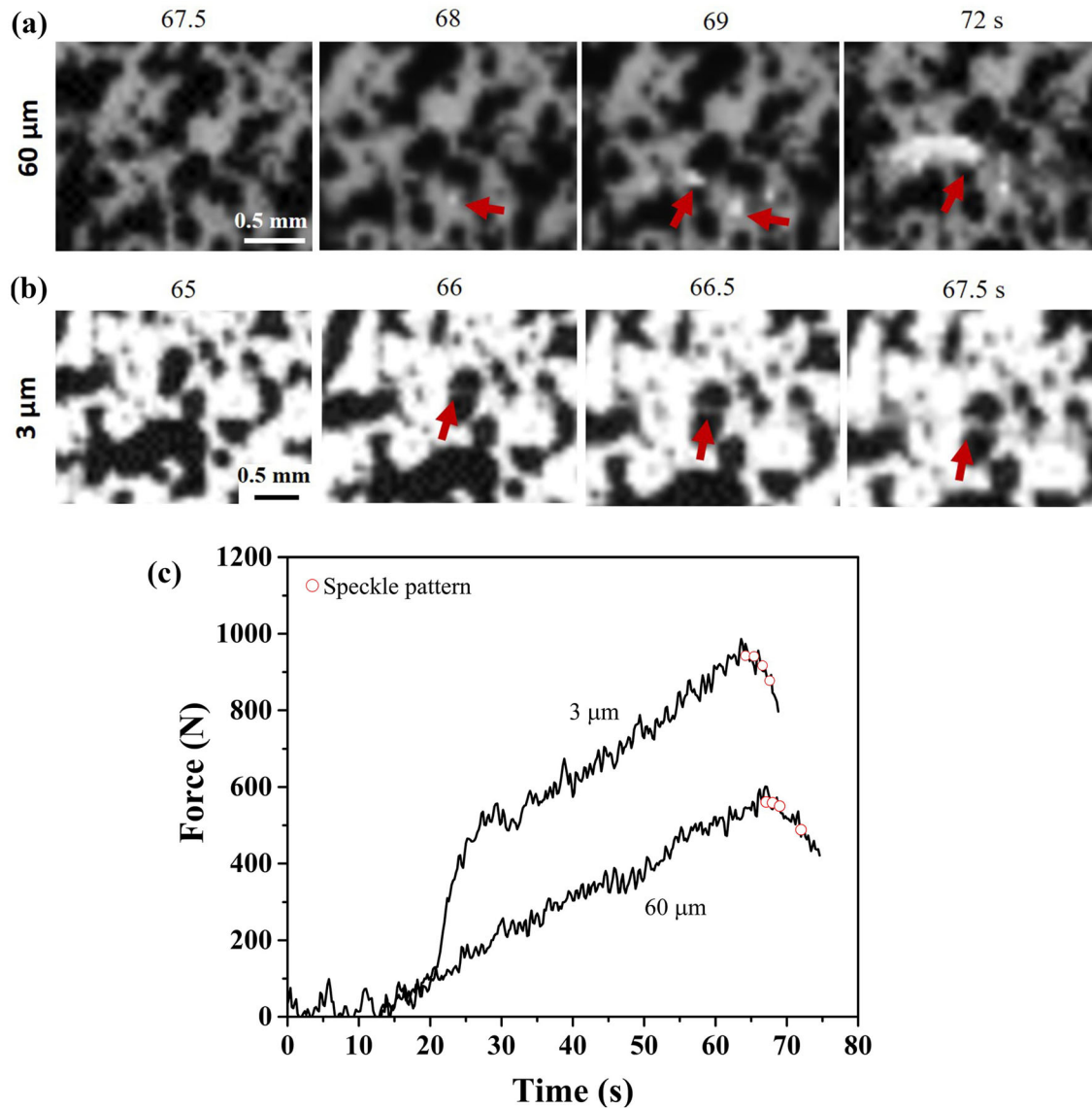


Fig. 5. Speckle patterns of the outer layer at different bending stages (a, b) and the corresponding force–time curves (c) in the coarse- and fine-grained materials (speckle irregularities show crack initiation just after reaching peak force).

Interestingly, there is also no significant evidence of void formation outside of the localized regions in any of the samples. This differs from tension testing, where it appears that void formation is involved in the triggering of macroscopic flow localization (void sheeting). We have recently suggested that the impact of grain size on the ductility in tension relates to the impact of grain size on void size.³¹ This is evidently a mechanism that is not present in bending, given that void formation clearly follows macroscopic localization of flow and

does not contribute materially to it. Finally, the similarity of the failure strains in compression for the two grain sizes shows that when the driving force for localization is sufficiently high, the grain boundaries present no real obstacle to its propagation and hence the grain size exerts little effect, even though the grain size is known to impact on twinning and twinning is involved in the present localization. The result is that the localization driven failure in bending displays negligible grain size sensitivity.

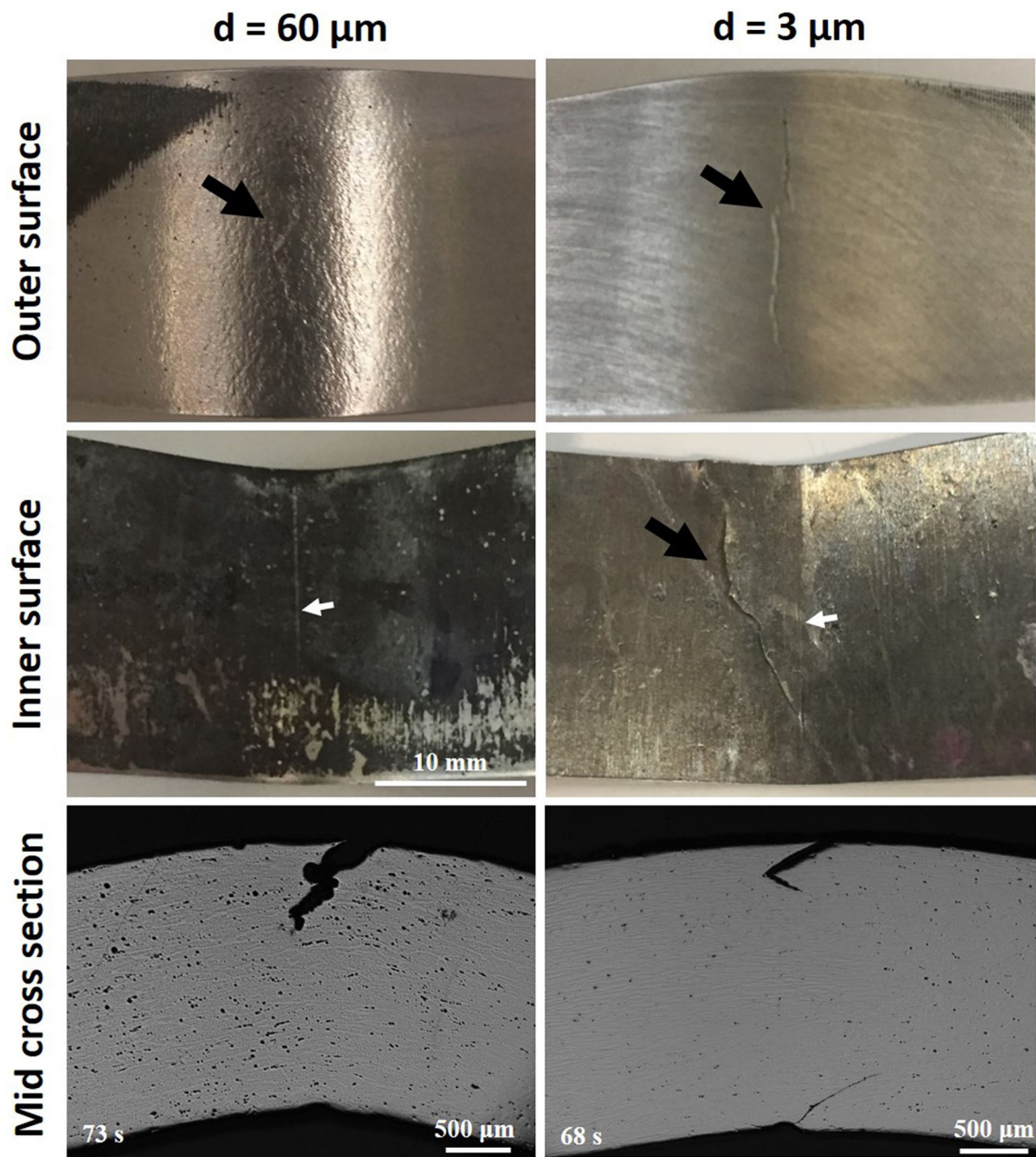


Fig. 6. Outer and inner surfaces and mid cross section (polished surfaces) of the bent samples with average grain sizes of $60 \mu\text{m}$ and $3 \mu\text{m}$, showing crack formation (punch mark shown by white arrows in the inner surface should be distinguished from cracks shown by black arrows).

Flow localization and subsequent crack propagation occurs preferentially along twin bands. The twin bands in the fine-grained material are narrower and shorter compared to those of the coarse-grained counterpart. This is associated with a reduction in twinning activity with grain refinement.^{34,35} However, this does not seem to influence crack initiation and propagation in bending. It should be mentioned that the secondary electron

images in Fig. 8b still show that the twin number density is higher than evident in the EBSD maps. This is due to indexing issues, which are more prevalent at smaller grain sizes. Evidently, only a few cracks form so only a relatively small number of twins, specifically double twins, maybe required for failure. More work is needed to be sure. The stress concentration at the tip of a crack also produces new twin boundaries, which can be consumed through

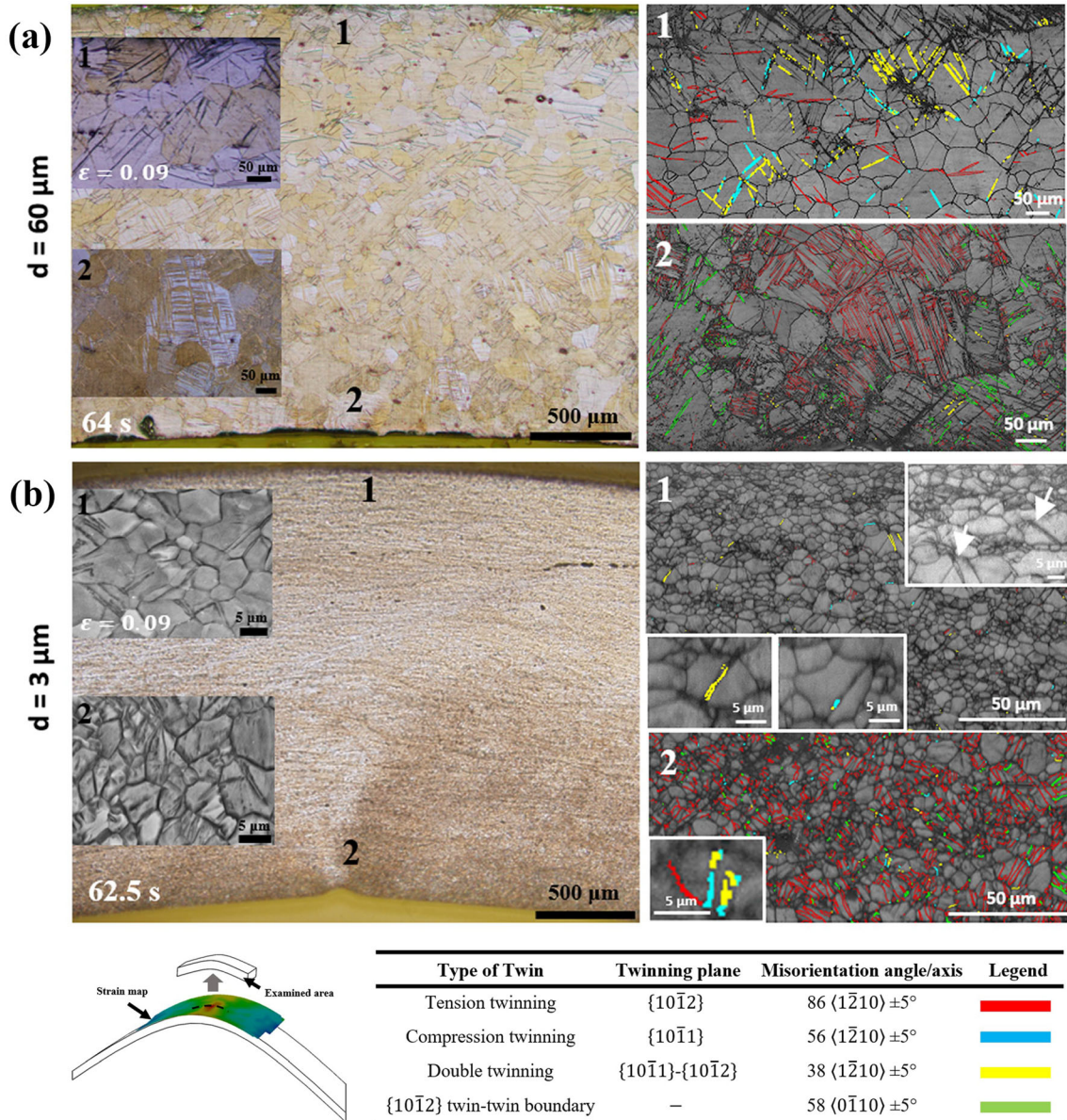


Fig. 7. Microstructures of the middle cross section of the highly bend deformed coarse-grained material (a) and fine-grained material (b) in tension zone (1) and compression zone (2) close to maximum force. The corresponding EBSD maps with step size of $0.1 \mu\text{m}$ in the tension and the compression zone show activity of various twinning systems. The examined area is shown in the schematic.

crack propagation. This propagation occurs in a zigzag path due to the activity of twin bands with two different orientations, which leads to the switching from one type to the other.

CONCLUSION

This study characterized bending behavior of a coarse- and fine-grained AZ31 magnesium alloy and the corresponding deformation micro-mechanisms. Microstructural and damage analysis leads to the following conclusions:

1. In the present tests, the bend forming limit of magnesium AZ31 does not improve with grain refinement. It remains to be seen how the present findings translate to larger punch radii.
2. The ductility in compression of wrought magnesium is insensitive to grain refinement. This impacts on the bend ductility because the inner 'side' of a bend experiences compression. Indeed, failure in the compression zone of bends was observed in the present study, for the fine-grained material.

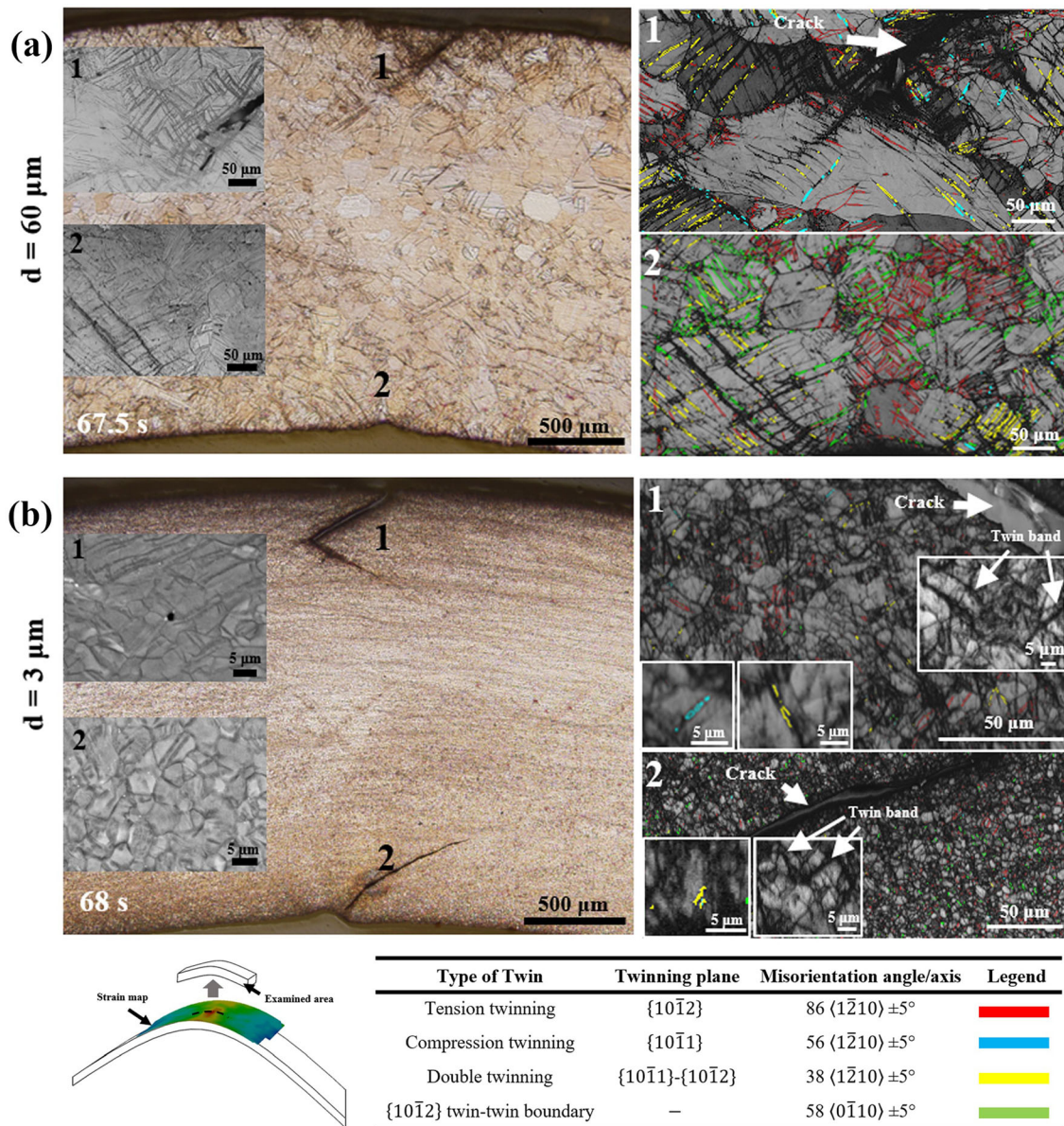


Fig. 8. Microstructures of the middle cross section of the bent coarse-grained material (a) and fine-grained material (b) in tension zone (1) and compression zone (2) after crack formation. The corresponding EBSD maps with step size of $0.1 \mu\text{m}$ in the tension and the compression zone show activity of various twinning systems. The examined area is shown in the schematic.

- Bend failure was seen to be controlled by flow localization and, unlike tension testing, void formation appeared not to be involved in the formation of shear localizations. Thus, the impact of grain size on void size that appears to be important in tension tests does not manifest itself in bending.
- It appears that in bending and in compression testing, the grain size has a negligible impact on the strain required for macroscopic flow localization to occur and that this is the critical condition controlling material failure.
- Twin bands consisting of $\{10\bar{1}1\}\{10\bar{1}2\}$ double twin boundaries appear to be responsible for flow localization and crack initiation in both the tension and the compression zones.

ACKNOWLEDGEMENTS

Financial support from a Deakin International Postgraduate Scholarship is gratefully acknowledged. The authors also acknowledge support from the Deakin Advanced Characterization Facility. S.H.M.A. thanks Prof. Bevis Hutchinson for productive discussions.

CONFLICT OF INTEREST

The authors declare that they have no conflict of interest.

ELECTRONIC SUPPLEMENTARY MATERIAL

The online version of this article (<https://doi.org/10.1007/s11837-020-04073-z>) contains supplementary material, which is available to authorized users.

REFERENCES

1. F. Zarandi and S. Yue, *Magnesium Sheet; Challenges and Opportunities* (INTECH Open Access Publisher, 2011).
2. S. R. Agnew, 2—Deformation mechanisms of magnesium alloys, *Advances in Wrought Magnesium Alloys*, (2012), pp 63–104.
3. G.T. Halmos, *Roll Forming Handbook* (Boca Raton: CRC Press, 2005).
4. J. Hu, Z. Marciniak, and J. Duncan, *Mechanics of Sheet Metal Forming* (Amsterdam: Elsevier Science, 2002).
5. J. Datsko and C.T. Yang, *J. Eng. Ind.* 82, 309 (1960).
6. M. R. Barnett, 6—Forming of magnesium and its alloys, in *Fundamentals of Magnesium Alloy Metallurgy*, (2013), pp. 197–231.
7. I. Aslam, B. Li, Z. McClelland, S.J. Horstemeyer, Q. Ma, P.T. Wang, and M.F. Horstemeyer, *J. Mater. Sci. Eng. A* 590, 168 (2014).
8. A. Ben-Artzy, L. G. Hector Jr and P. E. Krajewski, in *Proceedings of the Magnesium Technology* (2010), pp. 69–75.
9. W. Wang, W. Zhang, W. Chen, G. Cui, and E. Wang, *J. Alloys Compd.* 737, 505 (2018).
10. S.A. Habib, J.T. Lloyd, C.S. Meredith, A.S. Khan, and S.E. Schoenfeld, *Int. J. Plast* 122, 285 (2019).
11. L. Jin, J. Dong, J. Sun, and A.A. Luo, *Int. J. Plast* 72, 218 (2015).
12. J. Singh, M.-S. Kim, and S.-H. Choi, *Int. J. Plast* 117, 33 (2019).
13. S. J. H. B. Li, A.L. Oppedal, P.T. Wang, M.F. Horstemeyer, TMS 2013, Annual Meeting and Exhibition, Supplemental Proceedings, 142nd.
14. L. Jin, J. Dong, A. Luo, R. Mishra, A. Sachdev, and W. Wu, *J. Mater. Sci.* 47, 3801 (2012).
15. C. Bruni, A. Forcellese, F. Gabrielli, and M. Simoncini, *J. Mater. Process. Technol.* 177, 373 (2006).
16. L. Wang, G. Huang, H. Zhang, Y. Wang, and L. Yin, *J. Mater. Process. Technol.* 213, 844 (2013).
17. M. Habibnejad-Korayem, M.K. Jain, and R.K. Mishra, *J. Mater. Sci. Eng. A* 648, 371 (2015).
18. M. Habibnejad-korayem, M.K. Jain, and R.K. Mishra, *J. Mater. Sci. Eng. A* 619, 378 (2014).
19. J. Bohlen, P. Dobroň, J. Swiostek, D. Letzig, F. Chmelík, P. Lukáč, and K.U. Kainer, *J. Mater. Sci. Eng. A* 462, 302 (2007).
20. H. Yu, Y. Xin, M. Wang, and Q. Liu, *J. Mater. Sci. Technol.* 34, 248 (2018).
21. D.L. Atwell, M.R. Barnett, and W.B. Hutchinson, *J. Mater. Sci. Eng. A* 549, 1 (2012).
22. A. Jain, O. Duygulu, D.W. Brown, C.N. Tomé, and S.R. Agnew, *J. Mater. Sci. Eng.* 486, 545 (2008).
23. N. Stanford and M.R. Barnett, *J. Alloys Compd.* 466, 182 (2008).
24. W. Yuan, S.K. Panigrahi, J.Q. Su, and R.S. Mishra, *Scr. Mater.* 65, 994 (2011).
25. H. Yu, C. Li, Y. Xin, A. Chapuis, X. Huang, and Q. Liu, *Acta Mater.* 128, 313 (2017).
26. L. Guo, Z. Chen, and L. Gao, *J. Mater. Sci. Eng. A* 528, 443 (2011).
27. C.M. Cepeda-Jiménez, J.M. Molina-Aldareguia, and M.T. Pérez-Prado, *Acta Mater.* 84, 443 (2015).
28. J.A. del Valle, F. Carreño, and O.A. Ruano, *Acta Mater.* 54, 4247 (2006).
29. D. Liu, Z. Liu, and E. Wang, *J. Mater. Sci. Eng. A* 612, 208 (2014).
30. Q. Miao, L.-X. Hu, H.-F. Sun, and E.-D. Wang, *Trans. Nonferrous Met. Soc. China* 19, 326 (2009).
31. S.H.M. Azghandi, M. Weiss, B.D. Arhatari, and M.R. Barnett, *J. Alloys Compd.* (2019). <https://doi.org/10.1016/j.jallcom.2019.152618>.
32. L. Balogh, S.R. Niezgoda, A.K. Kanjarla, D.W. Brown, B. Clausen, W. Liu, and C.N. Tomé, *Acta Mater.* 61, 3612 (2013).
33. P. Chen, F. Wang, J. Ombogo, and B. Li, *J. Mater. Sci. Eng. A* 739, 173 (2019).
34. M.R. Barnett, *J. Mater. Sci. Eng. A* 464, 8 (2007).
35. J. Koike, *Metall. Mater. Trans. A* 36, 1689 (2005).

Publisher's Note Springer Nature remains neutral with regard to jurisdictional claims in published maps and institutional affiliations.